# Reduction of intrinsic critical current density under a magnetic field along the hard axis of a free layer in a magnetic tunnel junction

Katsuya Miura,[1,2,3,*] Ryoko Sugano,[1,4] Masahiko Ichimura,[1,4] Jun Hayakawa,[1] Shoji Ikeda,[2,3] Hideo Ohno,[2,3] and Sadamichi Maekawa[4,5]

[1]*Advanced Research Laboratory, Hitachi, Ltd., 1-280 Higashi-koigakubo, Kokubunji-shi, Tokyo 185-8601, Japan*

[2]*Laboratory for Nanoelectronics and Spintronics, Research Institute of Electrical Communication, Tohoku University, 2-1-1 Katahira, Aoba-ku, Sendai 980-8577, Japan*

[3]*Center for Spintronics Integrated Systems, Tohoku University, 2-1-1 Katahira, Aoba-ku, Sendai 980-8577, Japan*

[4]*JST, CREST, 5, Sanbancho, Chiyoda-ku, Tokyo 102-0075, Japan*

[5]*Advanced Science Research Center, Japan Atomic Energy Agency, Tokai, 319-1195, Japan*

(Received 22 March 2011; revised manuscript received 24 June 2011; published 23 November 2011)

We investigated the effect of a magnetic field along a hard in-plane axis $H_{\rm hard}$ on a current-induced magnetization switching (CIMS) in magnetic tunnel junctions (MTJs). Since $H_{\rm hard}$ causes the effective field to tilt away from the easy axis, we evaluated the $H_{\rm hard}$ dependence of two contributing factors in CIMS [the intrinsic critical current density ($J_{c0}$) and the thermal stability factor ($E/k_BT$)] as functions of the tilting angle ($\theta_H$). Both measurements and numerical simulations showed that the presence of $H_{\rm hard}$ can reduce $J_{c0}$ by more than the amount estimated by Slonczewski's polarization function $g(\theta)$ by an order of magnitude and that $E/k_BT$ is independent of $\theta_H$. These findings suggest that the effect of $H_{\rm hard}$ mainly appears in the dynamic properties due to the nonconservative force of the spin-transfer torque based on the Slonczewski's model. A simple stability analysis demonstrated that the tilt of the magnetization direction away from the easy axis caused by the presence of $H_{\rm hard}$ induces an imbalance between the spin-transfer and damping torques and that applying a current achieves the further tilted stable state. Achievement of this stable state can be interpreted as the suppression of the effect of the effective demagnetization field ($H_d^*$). Therefore the major reduction in $J_{c0}$ is due to the suppression of $H_d^*$ caused by the presence of $H_{\rm hard}$.

DOI: 10.1103/PhysRevB.84.174434 PACS number(s): 75.78.−n, 75.60.Jk

## I. INTRODUCTION

The spin-transfer torque (STT) phenomena in magnetic nanostructures predicted by Slonczewski[1] and Berger[2] produce several types of magnetic dynamics, including current-induced magnetization switching (CIMS). In nanosized magnetic tunnel junctions (MTJs),[3,4] CIMS between two static magnetic states has been demonstrated for various types of free layers. For spintronic device applications, STT in MTJs provide a promising mechanism for manipulating magnetic moments.[5,6] Compared with other structures, MTJs with a CoFeB/MgO/CoFeB structure[7,8] are attractive because they simultaneously exhibit high tunnel magnetoresistance (TMR) ratios[9] and CIMS.[10,11] For MTJs to be applied to the memory elements of nonvolatile logic circuits[12,13] and nonvolatile memory such as STT random access memory (STT-RAM),[14–17] the critical current density $J_c$ must be reduced.

Reduction in $J_c$ can be achieved by focusing on two factors, thermal stability factor $E/k_BT$ and intrinsic critical current density $J_{c0}$, because $J_c$ can be expressed as a combination of these factors.[18–21] Here, $E$ is the energy barrier between two static magnetic states, $k_B$ is the Boltzmann constant, and $T$ is the temperature. Note that $E/k_BT$ reflects a wide range of the magnetostatic energy landscape and that $J_{c0}$ reflects the dynamics of magnetization in a small energy range around the stable state, balanced between STT and damping/dissipation.

Inokuchi *et al.*[22] found that $J_{c0}$ in MTJs decreases when a magnetic field is applied along the hard in-plane axis of the free layer $\mathbf{H}_{\rm hard}$ in MTJs and that $E/k_BT$ is independent of $\mathbf{H}_{\rm hard}$. They indicated that the decrease in $J_{c0}$ was caused by an increase in Slonczewski's polarization function $g(\theta)$ (in-plane torque), which indicates the spin efficiency. Wang *et al.*[23] found that the perpendicular torque strongly depends on the angle of the free layer in their STT analysis. The relationship between the switching process and these torques, however, has not been fully clarified.

In the absence of an external magnetic field, $J_{c0}$ in MTJs with in-plane anisotropy and large demagnetization energy is expressed as[24]

$$J_{c0} \approx \alpha\gamma e M_s H_d^* t/\mu_B g(\theta), \tag{1}$$

where $\alpha$ is the magnetic damping constant, $\gamma$ is the gyromagnetic ratio, $e$ is the elementary charge, $M_s$ is the saturation magnetization, $H_d^*$ is the effective demagnetization field, $t$ is the thickness of the free layer, and $\mu_B$ is the Bohr magneton. Equation (1) implies that the reduction in $J_{c0}$ is due to an increase in $g(\theta)$ and/or decrease in $H_d^*$.

To determine which one is more effective for reducing in $J_{c0}$ in the presence of $\mathbf{H}_{\rm hard}$, we first measured $J_{c0}$ and $E/k_BT$ as functions of the mutual angle $\theta_H$ between the pinned layer and the free layer in MTJs. This angle is interpreted as the angle at which the effective field $\mathbf{H}_{\rm eff}$ tilts away from the easy axis due to the presence of $\mathbf{H}_{\rm hard}$. Next, we performed numerical simulation and simple stability analysis of CIMS of the free layer using a macrospin model to investigate the dynamic properties associated with the balance between STT based on the Slonczewski's model and the damping.

 

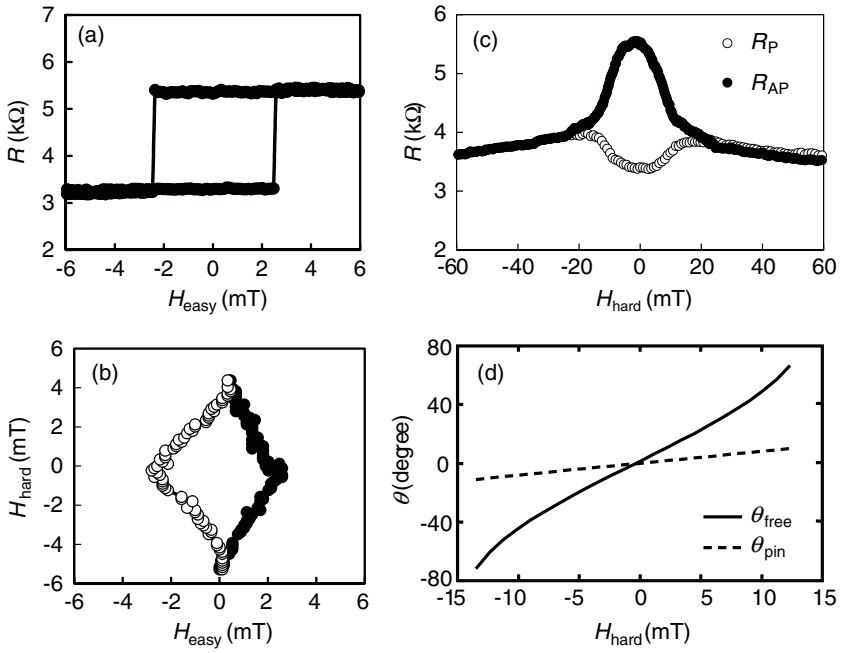


FIG. 1. (a) Dependence of $R$ on $H_{easy}$ at $H_{hard} = 0$ from which we obtained $R_P$ of 3.2 kΩ, $R_{AP}$ of 5.4 kΩ, and the TMR ratio of 69%. (b) Asteroid curves of MTJ. Open (solid) circles represent fields for switching from AP to P (P to AP) state. Extra magnetic field at origin of asteroid curves is small because center of asteroid curves corresponds approximately to origin. (c) Dependencies of $R_P$ and $R_{AP}$ on $H_{hard}$ at the applied current of 10 $\mu$A were used to determine $\theta_{free}$ and $\theta_{pin}$. Open (solid) circles represent $R_P$ ($R_{AP}$). (d) $\theta_{free}$ and $\theta_{pin}$ as functions of $H_{hard}$.

We obtained the following results: (i) from the experimental results at $\theta_H = 9^\circ$, $J_{c0}$ decreased by more than 20%, exceeding the contribution of the polarization function $g(\theta)$, which was estimated to be 0.4%, and that $E/k_BT$ was independent of $\theta_H$. (ii) Numerical simulations reproduced these experimental results. The stability analysis showed that the initial stable state with the tilted magnetization due to the presence of $\mathbf{H}_{hard}$ created an imbalance in the STT and damping torque, in contrast to the state without tilting under the easy-axis applied field ($H_{easy}$). This $H_{hard}$-induced imbalance produced further tilting of the magnetization in the stable state depending on the external current density $J$. Achievement of this stable state can be interpreted as the suppression of $H_d^*$. Therefore the major reduction in $J_{c0}$ can be attributed to the suppression of $H_d^*$ due to the presence of $H_{hard}$, indicating that $J_{c0}$ is sensitive to $H_{hard}$ rather than $H_{easy}$.

This paper is organized as follows. In Sec. II, we describe the sample preparation. Section III presents and discusses our experimental results. In Sec. IV, we discuss the Landau-Lifshitz-Gilbert equation with the spin-transfer torque term (LLGS) based on the macrospin model. Section IV A presents the numerical results. Section IV B discusses the dynamic properties associated with the balance between STT and the damping around the tilted $\mathbf{H}_{eff}$ as revealed by the stability analysis. In Sec. IV C, we discuss the effect of the change in the dynamic properties on $J_{c0}$. We conclude in Sec. V with a summary of the key points and a brief remark.

## II. SAMPLE PREPARATION

We prepared MTJs with a single free layer of $Co_{40}Fe_{40}B_{20}$ (2.0 nm) fabricated on a coplanar wave guide to enable application of a fast pulse current. The starting multilayers were deposited on sapphire substrates using radio-frequency magnetron sputtering with a base pressure of $10^{-7}$ Pa. The order of the film layers was, starting from the substrate, Ta(5)/Ru(10)/Ta(5)/NiFe(5)/MnIr(8)/CoFe(4)/Ru(0.8)/$Co_{40}Fe_{40}B_{20}$(5)/MgO(0.8)/$Co_{40}Fe_{40}B_{20}$(2)/Ta(5)/Ru(5) (in nm). They were then microstructured into MTJs with a dimension of 100 × 200 nm using electron beam lithography and Ar-ion milling. The completed MTJs were annealed at 300 °C for one hour in a $10^{-4}$-Pa vacuum under a magnetic field of 400 mT.

## III. EXPERIMENTAL RESULTS

First, we measured the dependence of resistance $R$ on $H_{easy}$ at $H_{hard} = 0$ and the asteroid curves of an MTJ. Figure 1(a) shows the dependence of resistance $R$ on $H_{easy}$ at $H_{hard} = 0$. The MTJs had two resistance states corresponding to their magnetization configurations. One was a parallel (P) configuration, which showed low resistance ($R_P$), and the other was an antiparallel (AP) configuration, which showed high resistance ($R_{AP}$). The switching between $R_P$ and $R_{AP}$ is clearly evident in Fig. 1(a).

Figure 1(b) shows the asteroid curves of the MTJ. The open (solid) circles represent the fields for switching from the AP to P (P to AP) state. The center of the asteroid curves corresponds approximately to the origin. These results indicate that extra magnetic fields at the origin, such as a stray field from the pinned layer, are small. These measurements showed that $R_P$ was 3.2 kΩ, $R_{AP}$ was 5.4 kΩ, and the TMR ratio was 69%.

Then, to determine the dependencies of $\theta_{free}$ and $\theta_{pin}$ on $H_{hard}$, we measured the $R_P$ and $R_{AP}$ of the MTJ as functions of $H_{hard}$ for an applied current of 10 $\mu$A. They are shown in Fig. 1(c). Here, $\theta_{free}$ ($\theta_{pin}$) is the angle between the direction of the magnetization of the free (pinned) layer of the MTJ and that of the in-plane easy axis. In this figure, the open (solid) circles represent the dependence of $R_P$ ($R_{AP}$) on $H_{hard}$. The $R_P$ increased as $|H_{hard}|$ increased up to around 20 mT because $\theta_H$ increased from 0 to $\pi/2$ with $|H_{hard}|$. The $R_{AP}$ decreased with $|H_{hard}|$ because $\theta_H$ decreased from $\pi$ to $\pi/2$. At around $|H_{hard}| = 20$ mT, the two resistance curves had the same value because $\theta_H$ reached $\pi/2$. The resistance values around $|H_{hard}| = 20$ mT were different from the average of $R_P$

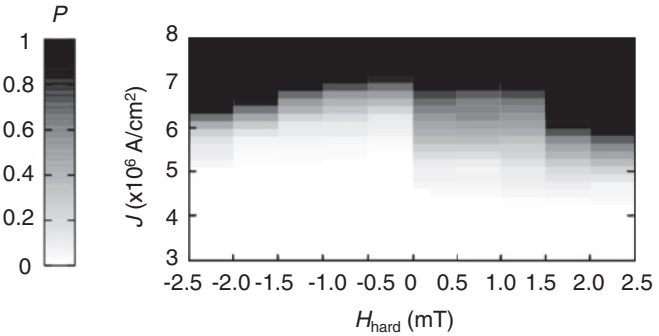


FIG. 2. Map of $P$ as a function of applied current density $J$ with $\tau_p = 100$ ns for various $H_{\rm hard}$ from which $J_{c0}$ and $E/k_BT$ were determined.

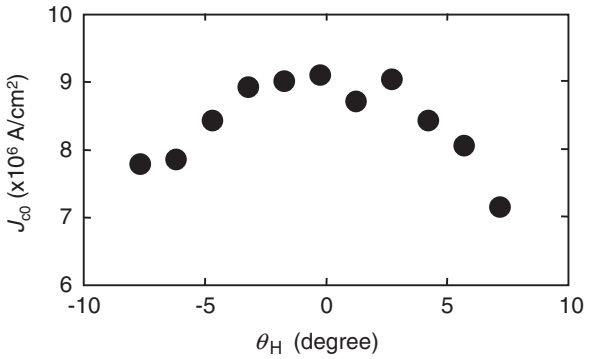


FIG. 3. $J_{c0}$ obtained from fitting of probability curves as a function of $\theta_H$.

and $R_{\rm AP}$ at $H_{\rm hard} = 0$. This is because $\theta_{\rm pin}$ gradually increased with $H_{\rm hard}$. From the resistance curves at $|H_{\rm hard}| > 20$ mT, which show the linear dependence on $H_{\rm hard}$, we estimated the dependence of $\theta_{\rm pin}$ on $H_{\rm hard}$. Assuming that the two resistance curves are proportional to $\cos(\theta_{\rm pin} - \theta_{\rm free})$, we estimated the dependence of $\theta_{\rm free}$ on $H_{\rm hard}$. The dependencies of $\theta_{\rm free}$ and $\theta_{\rm pin}$ on $H_{\rm hard}$ are shown in Fig. 1(d).

Next, we measured the switching probability ($P$) of CIMS as a function of the current density at various $H_{\rm hard}$ to obtain the dependencies of $J_{c0}$ and $E/k_BT$ on $\theta_H$. We applied a magnetic field up to $|H| = 2.5$ mT. Note that the mutual angle $\theta_H$ approximately corresponds to $\theta_{\rm free}$ in this region because the change in $\theta_{\rm pin}$ is much smaller than that in $\theta_{\rm free}$, as shown in Fig. 1(d). Figure 2 shows a map of $P$ as a function of applied current density $J$ with $\tau_p = 100$ ns for various $H_{\rm hard}$, where $\tau_p$ is the pulse duration time of the applied current. At each $H_{\rm hard}$, $P$ was expressed using the following equation, which is theoretically predicted in the thermal activation regime:[18–21]

$$P = 1 - \exp\left\{ -\frac{\tau_p}{\tau_0} \exp\left[ -\frac{E}{k_BT}\left(1 - \frac{J}{J_{c0}}\right)\right]\right\}, \qquad (2)$$

where $\tau_0$ is the inverse of the attempt frequency and is assumed to be 1 ns. We can determine $J_{c0}$ and $E/k_BT$ at each $H_{\rm hard}$ from the fitting based on this equation. The determined $J_{c0}$ and $E/k_BT$ are plotted as functions of $\theta_H$ in Figs. 3 and 4 using the relationship between $H_{\rm hard}$ and $\theta_H$, which, as mentioned above, approximately corresponds to $\theta_{\rm free}$ in this magnetic field region. The $J_{c0}$ dropped from 9 to 7 $\times$ $10^6$ A/cm$^2$ when $|\theta_H|$ increased from 0 to 9 degrees. The $E/k_BT$ had no specific dependence on $|\theta_H|$.

We investigated whether the decrease in $J_{c0}$ arises only from the increase in $g(\theta)$ by using[25]

$$g(\theta) = \frac{\eta}{2}(1 + \eta^2 \cos\theta), \qquad (3)$$

where $\eta$ is the spin-polarization factor, to estimate $g(\theta)$. We found that estimated $g(\theta)$ increased by 0.4% when $\theta_H$ increased from 0° to 9°, which is sufficiently small to explain the decrease in $J_{c0}$. Slonczewski and Sun modified Eq. (3) to include the inelastic tunneling effect.[26] They found that the polarization function does not depend on $\theta$. Hence, the reduction in $J_{c0}$ cannot be explained by the increase in the polarization function. Our measurements revealed the following properties of $J_{c0}$ and $E/k_BT$. The $J_{c0}$ under the $H_{\rm hard}$ condition is reduced by more than the contribution of the polarization function, and $E/k_BT$ does not vary with $H_{\rm hard}$. Therefore the reduction in $J_{c0}$ is possibly caused by other effects, for example, the change in the dynamic properties due to the current-induced STT. We investigated this possibility through the simulation and the simple stability analysis.

## IV. SIMULATIONS AND DISCUSSION

In this section, we discuss the reduction in $J_{c0}$ due to the presence of $H_{\rm hard}$ in terms of two theoretical treatments based on the macrospin model.[24] We performed the systematic numerical simulation of CIMS and stability analysis to determine the equilibrium magnetization configurations evaluated from the balancing condition between current-induced STT and damping under $H_{\rm hard}$ condition. Although this approach is similar to that used by Sun[24] for an "on-axis" geometry, in which both the applied magnetic field and the magnetization direction of pinned layer are along the easy axis, we used a different arrangement. Only the magnetization of the pinned layer was along the easy axis. The applied magnetic field was in the hard in-plane direction.

We began our analysis by using the LLGS equations.[1] Using the macrospin model[24] shown in Fig. 5(a), we treated magnetization $\mathbf{M}$ as a model of a uniformly magnetized free layer (F) in MTJs with volume $V_0$ and saturation magnetization $M_s$. The MTJs were assumed to have a uniaxial anisotropy field $\mathbf{H}_k$. We analyzed the magnetization dynamics of unit vector $\mathbf{m} = \mathbf{M}/M_s = (\theta, \varphi)$ with two degrees of freedom, polar $\theta$

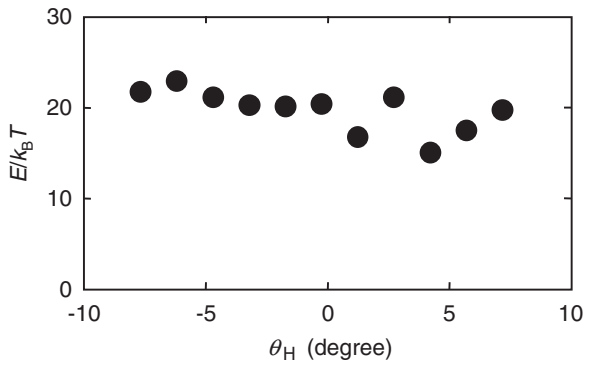


FIG. 4. $E/k_BT$ obtained from fitting of probability curves as a function of $\theta_H$.

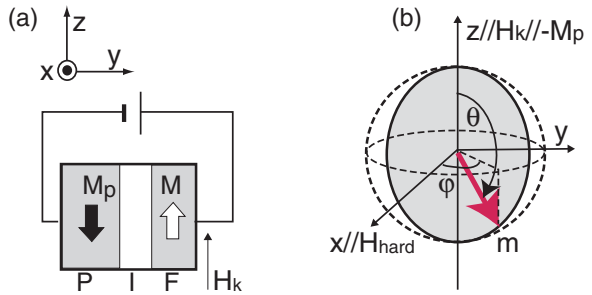


FIG. 5. (Color online) (a) Schematic diagram of MTJ device consisting of pinned layer (P), insulating barrier (I), and free layer (F). (b) Polar coordinates of magnetization vector **m** and applied field $\mathbf{H}_{\text{hard}}$.

and azimuth $\varphi$ angles, as shown in Fig. 5(b). The $\mathbf{H}_k$ (easy axis) was along the $+z$ direction, and the fixed magnetization direction $\mathbf{M}_p$ in the pinned layer (P) was along the $-z$ direction ($\mathbf{H}_k \| -\mathbf{M}_p \| \mathbf{z}$). The magnetic field $\mathbf{H}_{\text{hard}}$ was applied along the $+x$ direction ($\mathbf{H}_{\text{hard}} \| \mathbf{x}$), and the demagnetization field $\mathbf{H}_d$ was along the $+y$ direction ($\mathbf{H}_d \| \mathbf{y}$).

For convenience in later discussion, we briefly describe the LLGS equation in the macrospin model. The spin-polarized current is restricted to the $+y$ direction. In the absence of thermal fluctuations, the LLGS equation is written in the following forms with the Gilbert damping constant $\alpha$:

$$\begin{pmatrix} \dot{\theta} \\ \dot{\varphi} \end{pmatrix} = \begin{pmatrix} -\alpha \sin\theta & -\sin\theta \\ 1 & -\alpha \end{pmatrix} \begin{pmatrix} \frac{1}{\sin\theta}\left(\frac{\partial \varepsilon}{\partial \theta}\right) \\ \frac{1}{\sin 2\theta}\left(\frac{\partial \varepsilon}{\partial \varphi}\right) - j \end{pmatrix}, \quad (4)$$

$$\epsilon = \frac{1}{2}(\sin^2\theta + h_d \sin^2\varphi \sin^2\theta - 2h_{\text{hard}} \sin\theta \cos\varphi). \quad (5)$$

In Eq. (4), $j[=(I_e/I_T)g(\theta)]$ corresponds to the current-induced STT, where $I_e$ is the applied current and $I_T(=2E_0\gamma_0 e/\mu_B)$ is the current scale. The $\epsilon$ is the potential energy normalized by the energy scale $E_0 = M_s H_k V_0/2$. The first term of the right side of Eq. (5) is the anisotropy term, the second term is the demagnetization energy term with demagnetization coefficient $h_d = M_s/\mu_0 H_k$, and the last term is the applied field energy with $h_{\text{hard}} = H_{\text{hard}}/H_k$.

### A. Numerical simulations

To investigate the reduction in $J_{c0}$ observed when a hard in-plane axis is present, we first performed Langevin simulation of Eq. (4) at finite temperature $T$ with an additional random fluctuation field $\mathbf{h}_{\text{fl}}(t)$ using a technique similar to that used previously,[27] in which the "antiparallel-to-parallel (AP-to-P)" CIMS of **m** was treated by referring to the direction of the spin-polarized current. The initial configurations were $\mathbf{m} \sim -\mathbf{z}$ to provoke AP-to-P CIMS. The parameter settings were set by $E_0 = 2.5\times10^4$ J/m$^3$, $T = 300$ K, $h_d = 21.7$, and $\alpha = 0.007$. The time step was set to 0.5–1.0 ps. The $h_{\text{hard}}$ varied from 0 to 1/3, which covered the field range in the experiments described in the previous section.

We simulated $N_s$ independent samples with fixed current density $J$. For each sample, a simulation was performed from $t = -10$ ns to $t = 0$ without STT to reach the initial condition of thermal equilibrium at $t = 0$. Systematically varying $J$, we numerically calculated the time evolution of

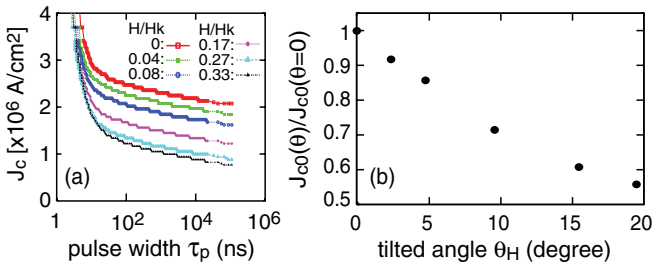


FIG. 6. (Color online) (a) $J_c$ as a function of $t_p$ of "AP-to-P" CIMS as a function of $J$ for various $h_{\text{hard}}$. (b) Extracted $J_{c0}$ as a function of $\theta_H$.

**m**. All the results were averaged over $N_s = 512$ different samples.

Figure 6(a) shows the switching current density $J_c$ as a function of the current pulse width $\tau_p$ for various values of $h_{\text{hard}}$. For comparison with the experimental results, $J_c$ was defined as the value of $J$ with probability $P = 1/2$ by using the criterion $P = (1 + \langle \mathbf{m} \cdot \mathbf{m}_p \rangle_{N_s})/2$, where $\langle \cdots \rangle_{N_s}$ indicates the average over $N_s$ samples and $\mathbf{m}_p$ is a unit vector of $\mathbf{M}_p$. Substituting this criterion for $J_c$ into Eq. (2), we found that CIMS in the thermal activation regime was accompanied by the logarithmic dependence of $\tau_p$: $J_c \propto \ln(\tau_p)$ and $J \ll J_{c0}$.[18–21] For $\tau_p > 10$ ns, $J_c$ clearly displayed a logarithmic dependence on $\tau_p$, indicating the thermal activation regime. The slopes of the curves for $\tau_p > 10$ ns are essentially independent of $h_{\text{hard}}$. This suggests that $E/k_BT$ is insensitive to $h_{\text{hard}}$. This agrees with the result presented in Fig. 4.

Using the inverse of attempt frequency $\tau_0$ (assumed to be 1 ns), we extracted $J_{c0}$ from a linear extrapolation in the thermal activation regime ($\tau_p > 10$ ns) in accordance with Eq. (2) for $J = J_c$. Figure 6(b) shows $J_{c0}$ as a function of $\theta_H$, which is the angle at which effective field $\mathbf{H}_{\text{eff}}$ is tilted away from the easy axis $\mathbf{H}_k$ and corresponds to the applied field through the relationship between $\theta_H$ and $h_{\text{hard}}$:

$$\sin\theta_H = h_{\text{hard}} = \frac{H_{\text{hard}}}{H_k}. \quad (6)$$

The reduction rate of $J_{c0}$ at $\theta_H \sim 10^\circ$ ($h_{\text{hard}} = 0.17$) was more than 20%. This is consistent with the result presented in Fig. 3 for $0^\circ < \theta < 10^\circ$. These results again suggest that the effect of the presence of $h_{\text{hard}}$ mainly appears in the dynamic properties due to a nonconservative force that cannot be estimated using the potential associated with $E/k_BT$.

### B. Balance of STT and damping around tilted direction of $\mathbf{H}_{\text{eff}}$

To investigate the dynamic properties of the magnetization of the free layer, we started from Eq. (4) in the absence of thermal fluctuations, as in the LLGS analysis. To simplify the analysis, we regarded the damping torque and STT as perturbations so that the enabled magnetization motion would conserve the magnetic energy, as in the unperturbed state. To eliminate the degree of freedom of $\varphi$, we took the averaged time derivative of $\theta$ over one period of motion for $\varphi$, which

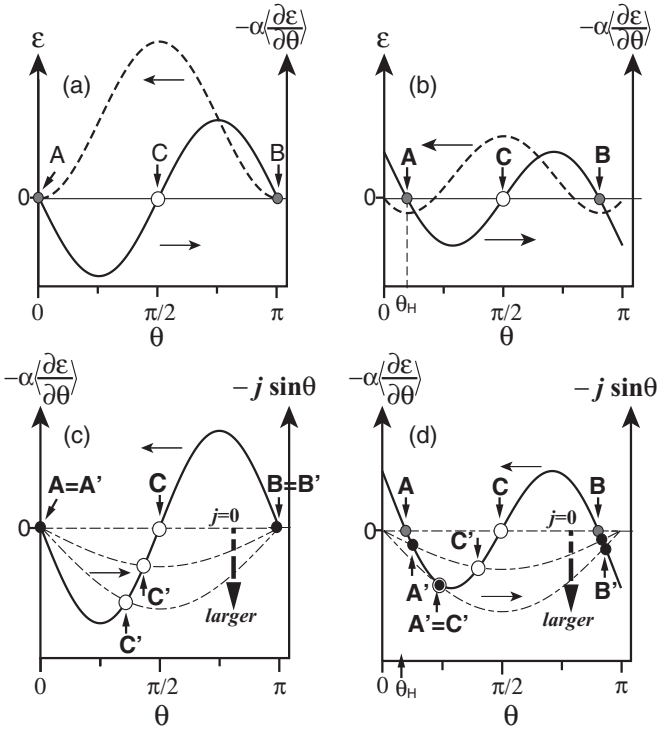


FIG. 7. $\theta$ dependence of damping torque ($-\alpha\langle\partial\varepsilon/\partial\theta\rangle$: solid line), STT ($j\sin\theta$: dash-dotted line), potential energy (dashed line), and the resulting equilibrium positions of magnetization including stable (solid circles) and saddle points (open circles). (a) $j = 0$ and $h_{\rm hard} = 0$, (b) $j = 0$ and $h_{\rm hard} \neq 0$, (c) $j \neq 0$ and $h_{\rm hard} = 0$, and (d) $j \neq 0$ and $h_{\rm hard} \neq 0$.

also conserved the magnetic energy. The averaged equation of motion is expressed as

$$\langle\dot{\theta}\rangle = -\alpha\left\langle\frac{\partial\varepsilon}{\partial\theta}\right\rangle + j\sin\theta, \tag{7}$$

$$\left\langle\frac{\partial\varepsilon}{\partial\theta}\right\rangle = [(1 + h_d\langle\sin^2\varphi\rangle)\sin\theta - h_{\rm hard}\langle\cos\varphi\rangle]\cos\theta. \tag{8}$$

The first and second terms on the right side of Eq. (7) represent the damping torque and STT, respectively. The balance between the damping torque and STT imposes the $\langle\dot{\theta}\rangle = 0$ condition.

We made the following assumption on the range of the degree of freedom $\varphi$ under the $h_{\rm hard}$ condition:

$$-\varphi_0 \leqslant \varphi \leqslant \varphi_0,\ 0 < \varphi_0 \ll 1. \tag{9}$$

Using the assumption (9), we can simplify Eq. (8) by using $\langle\sin^2\varphi\rangle = 0$ and $\langle\cos\varphi\rangle = 1$. Our assumption is supported by numerical simulation, as discussed below (see Fig. 9).

Figure 7 schematically summarizes the $\theta$ dependence of the damping torque ($-\alpha\langle\partial\varepsilon/\partial\theta\rangle$) and STT ($j\sin\theta$) and the resulting equilibrium positions of magnetization (including stable and saddle points), in the following order: (a) $j = 0$ and $h_{\rm hard} = 0$, (b) $j = 0$ and $h_{\rm hard} \neq 0$, (c) $j \neq 0$, and $h_{\rm hard} = 0$ and (d) $j \neq 0$ and $h_{\rm hard} \neq 0$. As shown in Figs. 7(a) and 7(b), the equilibrium magnetization was determined only by the magnetostatic energy and is equivalent to the result from the saddle point conditions of $\partial\varepsilon/\partial\theta = 0$ and $\partial\varepsilon/\partial\varphi = 0$.[28,29] For $h_{\rm hard} = 0$ [see Fig. 7(a)], two stable states (solid circles) are located at the north (A) and the south (B) poles ($\sin\theta = 0$), and a saddle point (open circle) at C. In the presence of $h_{\rm hard}$ [see Fig. 7(b)], stable states A and B move toward the applied field direction ($\mathbf{H}_{\rm hard}\|\mathbf{x}$), while saddle point C remains at $\theta = \pi/2$. Stable states A and B are determined by the condition $\sin\theta = h_{\rm hard}$, which in our simplification is $\langle\sin^2\varphi\rangle = 0$ and $\langle\cos\varphi\rangle = 1$. The direction of the damping torque on the $\theta$ axis is symmetric around the equilibrium positions (A, B, and C) and oriented toward the stable state, both for Figs. 7(a) and 7(b).

Next, we took into account the contribution of STT driven by $J$. Figures 7(c) and 7(d) show the graphical solutions of Eq. (7) without and with $h_{\rm hard}$, respectively. When $h_{\rm hard} = 0$, in contrast to Fig. 7(b), stable state A' (B') remains at $\theta = 0$ ($\theta = \pi$), and saddle point C' moves away from the direction of $\theta = \pi$. In other words, the saddle point C' also moves toward the direction of the nonreversed magnetization of $\theta = 0$. This means that the displacement of C' accompanies the destabilization of nonreversed state A'. Since, for $h_{\rm hard} = 0$, states A' and B' are identical to A and B, the direction of the damping torque on the $\theta$ axis is symmetric around the stable positions (A and B) and oriented toward the stable states. Note that the direction of the damping torque at the saddle point C' is oriented toward stable state A unidirectionally. In the presence of $h_{\rm hard}$, as shown in Fig. 7(d), the stable states A' and B' move toward the direction of $\theta = \pi$ due to STT. When $J$ increases, the destabilization of the nonreversed state A' is enhanced because stable state A' and saddle point C' become closer. After A' and C' merge into a single state, A' and C' disappear. This merged state means that nonreversed (initial) state A' can no longer remain stable. When $J$ is so large that A' and C' disappear, the unique solution that B' remains as the stable state corresponds to the reversed magnetization. The direction of the damping torque at A' and B' is oriented toward A and B, respectively, that at C' is oriented toward A.

To quantitatively discuss the above schematic interpretation, we evaluated numerically magnetization equilibrium positions $\theta$ as functions of current density $J$, as shown in Fig. 8. Here, we treat the limiting case of $\varphi_0 \to 0$ from Eqs. (7) and (8). These equilibrium positions of magnetization were obtained from two intersecting surfaces: one surface of $\langle\dot{\theta}\rangle$ as a function of $J(\propto j)$ and $\theta$ with a surface constraint of $\langle\dot{\theta}\rangle = 0$. The solid and dash-dotted lines represent the case for $\theta_H = 10^\circ$, and the dashed line represents the case for $\theta_H = 0^\circ$ ($h_{\rm hard} = 0$). For $\theta_H = 10^\circ$, the solid line denotes the saddle point (C') and the dash-dotted line denotes the stable and nonreversed state (A') as a function of $J$, corresponding to equilibrium states C' and A' in Fig. 7(d). Since the region $\langle\dot{\theta}\rangle \leqslant 0$ maps onto the region surrounded by the solid and dash-dotted lines, the magnetization cannot reverse in this region. In addition, if $\langle\dot{\theta}\rangle \geqslant 0$, the state around A' converges to the stable nonreversed state A', and the reverse and nonreverse regions are separated by the white and gray regions.

### C. $J_{c0}$ in the presence of $H_{\rm hard}$

Here, we discuss the reduction of $J_{c0}$ caused by the presence of $h_{\rm hard}$. Since $J_{c0}$ is the maximum value of $J_c$, $J_{c0}$ in the case of $\theta_H = 10^\circ$ is determined by $J_c$, which corresponds to the

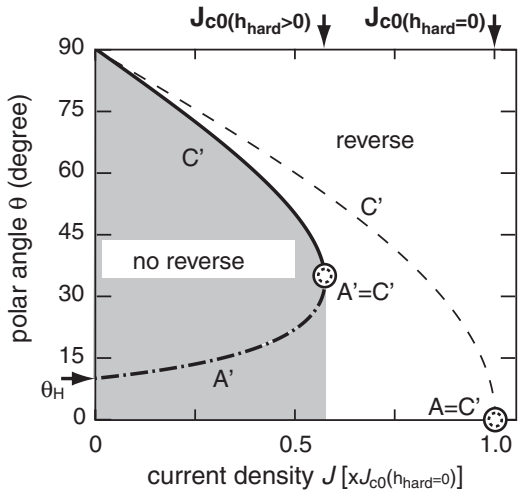


FIG. 8. Equilibrium positions $\theta$ of magnetization as functions of $J$ in the limiting case of $\varphi_0 \to 0$ from Eqs. (7) and (8). Solid and dash-dotted lines show stable states and saddle points for hard in-plane axis applied field at $\theta_H = 10^\circ$ in limit of $\varphi_0 = 0^\circ$. Dashed line represents saddle point at $h_{\rm hard} = 0$.

merging point A' = C'. In the limiting case of $\theta_H \to 0^\circ$, the solid line for $\theta_H = 10^\circ$ in Fig. 8 approaches the dashed line, and the dash-dotted line approaches the horizontal axis. As a result, the stable state for $h_{\rm hard} = 0$ can be regarded as a state of continuous deformation for $h_{\rm hard} \neq 0$. Note that, for $\theta_H \neq 0$, dash-dotted line A' has a positive gradient because the $J$ dependence of $\langle\dot{\theta}\rangle$ has the form of $\sin\theta$ from Eq. (7). This positive gradient should greatly reduce $J_{c0}$. In the limit $\varphi \to 0$, $J_{c0}$ is approximately described using $h_{\rm hard}$:

$$\frac{J_{c0(h_{\rm hard})}}{J_{c0(h_{\rm hard}=0)}} > 1 - h_{\rm hard}^{2/3}. \tag{10}$$

Now we discuss the validity of the assumption underlying Eq. (9) on the basis of the simulation results. Figure 9 shows the time-averaged distribution of degree of freedom $\varphi$ immediately below $J_c$ for $\theta_H = 2.5^\circ$ (dash-dotted line), $10^\circ$ (dotted), and $20^\circ$ (solid). For all $\theta_H$, distinct peaks appeared at $\varphi = 0^\circ$. The range of $\varphi$ was at most $\varphi < \varphi_0 \sim 15^\circ$. This result supports the assumption underlying Eq. (9). Stable state A' remained at the pole for $h_{\rm hard} = 0$ even when $J$ increased, so the trajectory of the small-$\theta$ precession always wrapped around the pole, indicating $\varphi_0 = \pi$. On the other hand, for $h_{\rm hard} \neq 0$, the stable state A' moved away from the pole, and the trajectory rarely wrapped around the north pole, as shown on the left in Fig. 9. This movement of stable state A' imposes a restriction on the range of $\varphi$ ($\varphi_0 \ll 1^\circ$), as shown on the right in Fig. 9. The restricted $\varphi$ affects the effective field, especially the effect of demagnetization field $h_d^*$ [$=h_d\langle\sin^2\varphi\rangle$ in Eq. (8)]. For $h_{\rm hard} = 0$, $h_d^* = h_d/2$ because the relationship $\langle\sin 2\varphi\rangle = 1/2$, while for $h_{\rm hard} \neq 0$, $h_d^* \ll h_d$ because $\langle\sin 2\varphi\rangle \ll 1$. As shown in Fig. 9, the width of the peak becomes narrow and the distribution density increases with an increase in $\theta_H$. This behavior reflects the coherent dynamics of the magnetization[30] observed experimentally.

The experimental and numerical results on the $J_{c0}$-$\theta_H$ relationship are plotted in Fig. 10. The solid curve shows the result of stability analysis using Eq. (10) in the limit $\varphi_0 \to 0$.

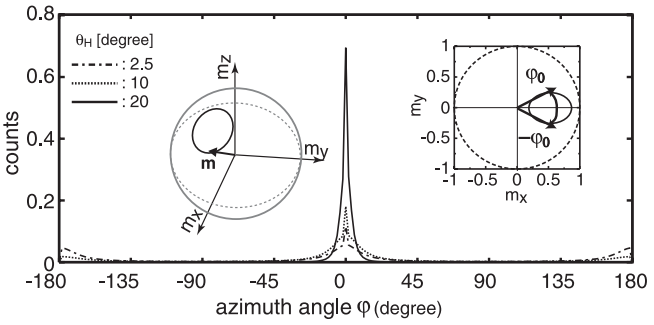


FIG. 9. Time-averaged distribution of degree of freedom $\varphi$ for $\theta_H = 2.5^\circ$, $10^\circ$, and $20^\circ$ immediately below $J_c$. Schematic trajectory with tilting of $\mathbf{H}_{\rm eff}$ accompanied by limited $\varphi_0$ is shown on the left, and its projection onto the $m_x m_y$-plane is shown on the right.

It gives the lower bound of $J_{c0}$. Both the simulation and the stability analysis results agree with experimental results.

Finally, we interpreted the reduction in $J_{c0}$ intuitively, considering the $J$ dependence of stable state A' related to the effect of demagnetization field $H_d^*$. In Sun's "on-axis" geometry, in which both magnetic field $H_{\rm easy}$ (not $H_{\rm hard}$) and the pinned direction were along the easy axis,[24] stable state A' stayed at the north pole independent of $J$, as in the zero-field case, and $H_d^*$ was given by $H_d/2$ independent of $H_{\rm easy}$. Sun thus predicted that $J_{c0} \propto H_k + H_d^* - H_{\rm easy}$. When $H_d^*$ is several orders of magnitude larger than $H_{\rm easy}$, $J_{c0}$ is dominated by $H_d^*$, leading to the approximation $J_{c0} \propto H_d^*$, as depicted in Eq. (1), even in the presence of $H_{\rm easy}$. Alternatively, in the presence of $H_{\rm hard}$ in place of $H_{\rm easy}$, $H_d^*$ significantly depends on $H_{\rm hard}$ and is largely suppressed ($H_d^* \ll H_d$) because stable state A' moves from the north pole to the south pole, exceeding $\theta_H$ as $J$ increases, as mentioned in the discussion of Fig. 9. This large suppression of $H_d^*$ is thought to be a factor for the reduction in $J_{c0}$. Therefore via the $H_{\rm hard}$-induced suppression of $H_d^*$, $J_{c0}$ becomes sensitive to $H_{\rm hard}$ rather than $H_{\rm easy}$. In the limit of $H_d^* \to 0$, $J_{c0}$ is given by Eq. (10) instead of Eq. (1).

## V. CONCLUSION

We investigated the effect of the magnetic field along the hard in-plane axis $H_{\rm hard}$ on current-induced magnetization switching (CIMS) in magnetic tunnel junctions (MTJs). Focusing on the fact that $\mathbf{H}_{\rm hard}$ causes tilting of the effective magnetic field $\mathbf{H}_{\rm eff}$ from the uniaxial anisotropy field $\mathbf{H}_k$, we

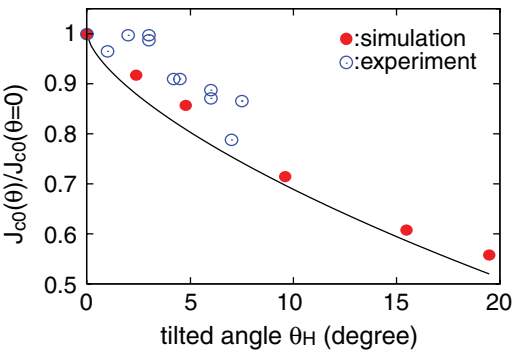


FIG. 10. (Color online) $J_{c0}$ as a function of $\theta_H$.

estimated the $H_{\text{hard}}$ dependence of two contributing factors in CIMS, $J_{c0}$ and $E/k_BT$, as functions of tilting angle $\theta_H$. Both measurements and numerical simulations showed that $H_{\text{hard}}$ can reduce $J_{c0}$ by an order of magnitude more than the estimated using Slonczewski's polarization function and that $E/k_BT$ is insensitive to $\theta_H$. These results suggest that $J_{c0}$ is not reduced by the variation of the magnetostatic condition, but by the dynamic properties due to the nonconservative force of STT. Simple stability analysis revealed that the initial stable tilted state of the magnetization from the easy axis due to the presence of $H_{\text{hard}}$ created an imbalance between the STT and damping torque, in contrast to the stable state without tilting under the $H_{\text{easy}}$ condition, in which the STT and damping are balanced. Applying a current causes a further tilted stable state. Achievement of this stable state A' can be interpreted as the suppression of $H_d^*$ due to a restriction on the range of $\varphi$, indicating that $J_{c0}$ is sensitive to $H_{\text{hard}}$ rather than to $H_{\text{easy}}$. Our observations of a major reduction in $J_{c0}$ indicate that change in the tilting angle due to the presence of $H_{\text{hard}}$ increases with $J$. These results present challenges to the design of STT devices controlled by $H_{\text{hard}}$.

## ACKNOWLEDGMENTS

The authors are grateful to M. Yamanouchi of Tohoku University for fruitful discussions. We thank S. Yabuuchi, H. Takahashi, and T. Hamada of Hitachi Advanced Research Laboratory for their productive suggestions. We also thank Y. A. Ono at RIKEN for his useful comments. This work was partly supported by the FIRST Program of JSPS and Research and Development for Next-Generation Supercomputing Project/Nanoscience Program from MEXT.

*katsuya.miura.aq@hitachi.com

[1] J. Slonczewski, J. Magn. Magn. Mater. **159**, L1 (1996).
[2] L. Berger, Phys. Rev. B **54**, 9353 (1996).
[3] S. Yuasa, T. Nagahama, A. Fukushima, Y. Suzuki, and K. Ando, Nat. Mater. **3**, 868 (2004).
[4] S. S. P. Parkin, C. Kaiser, A. Panchula, P. M. Rice, B. Hughes, M. Samant, and S.-H. Yang, Nat. Mater. **3**, 862 (2004).
[5] I. N. Krivorotov, N. C. Emley, J. C. Sankey, S. I. Kiselev, D. C. Ralph, and R. A. Buhrman, Science **307**, 228 (2005).
[6] J. Z. Sun and D. C. Ralph, J. Magn. Magn. Mater. **320**, 1227 (2008).
[7] D. D. Djayaprawira, K. Tsunekawa, M. Nagai, H. Maehara, S. Yamagata, N. Watanabe, S. Yuasa, Y. Suzuki, and K. Ando, Appl. Phys. Lett. **86**, 092502 (2005).
[8] J. Hayakawa, S. Ikeda, F. Matsukura, H. Takahashi, and H. Ohno, Jpn. J. Appl. Phys. **44**, L587 (2005).
[9] S. Ikeda, J. Hayakawa, Y. Ashizawa, Y. M. Lee, K. Miura, H. Hasegawa, M. Tsunoda, F. Matsukura, and H. Ohno, Appl. Phys. Lett. **93**, 082508 (2008).
[10] Z. Diao, D. Apalkov, M. Pakala, Y. Ding, A. Panchula, and Y. Huai, Appl. Phys. Lett. **87**, 232502 (2005).
[11] J. Hayakawa, S. Ikeda, Y. M. Lee, R. Sasaki, T. Meguro, F. Matsukura, H. Takahashi, and H. Ohno, Jpn. J. Appl. Phys. **44**, L1267 (2005).
[12] S. Matsunaga, J. Hayakawa, S. Ikeda, K. Miura, H. Hasegawa, T. Endoh, H. Ohno, and T. Hanyu, Appl. Phys. Exp. **1**, 091301 (2008).
[13] S. Matsunaga, K. Hiyama, A. Matsumoto, S. Ikeda, H. Hasegawa, K. Miura, J. Hayakawa, T. Endoh, H. Ohno, and T. Hanyu, Appl. Phys. Exp. **2**, 023004 (2009).
[14] M. Hosomi, H. Yamagishi, T. Yamamoto, K. Bessho, Y. Higo, K. Yamane, H. Yamada, M. Shoji, H. Hachino, C. Fukumoto, H. Nagao, and H. Kano, IEDM Tech. Dig, 459 (2005).
[15] T. Kawahara, R. Takemura, K. Miura, J. Hayakawa, S. Ikeda, Y. M. Lee, R. Sasaki, Y. Goto, K. Ito, T. Meguro, F. Matsukura, H. Takahashi, H. Matsuoka, and H. Ohno, IEEE J. Solid-State Circuits **43**, 109 (2008).
[16] R. Takemura, T. Kawahara, K. Miura, H. Yamamoto, J. Hayakawa, N. Matsuzaki, K. Ono, M. Yamanouchi, K. Ito, H. Takahashi, S. Ikeda, H. Hasegawa, H. Matsuoka, and H. Ohno, IEEE J. Solid-State Circuits **45**, 869 (2010).
[17] K. Tsuchida, T. Inaba, K. Fujita, Y. Ueda, T. Shimizu, Y. Asao, T. Kajiyama, M. Iwayama, K. Sugiura, S. Ikegawa, T. Kishi, T. Kai, M. Amano, N. Shimomura, H. Yoda, and Y. Watanabe, ISSCC Tech, Dig., 258 (2010).
[18] J. Z. Sun, T. S. Kuan, J. A. Katine, and R. H. Koch, Proc. SPIE **5359**, 445 (2004).
[19] Z. Li and S. Zhang, Phys. Rev. B **69**, 134416 (2004).
[20] R. H. Koch, J. A. Katine, and J. Z. Sun, Phys. Rev. Lett. **92**, 088302 (2004).
[21] D. Lacour, J. A. Katine, N. Smith, M. J. Carey, and J. R. Childress, Appl. Phys. Lett. **85**, 4681 (2004).
[22] T. Inokuchi, H. Sugiyama, Y. Saito, and K. Inomata, Appl. Phys. Lett. **89**, 102502 (2006).
[23] C. Wang, Y.-T. Cui, J. Z. Sun, J. A. Katine, R. A. Buhrman, and D. C. Ralph, Phys. Rev. B **79**, 224416 (2009).
[24] J. Z. Sun, Phys. Rev. B **62**, 570 (2000).
[25] J. C. Slonczewski, Phys. Rev. B **71**, 024411 (2005).
[26] J. C. Slonczewski and J. Z. Sun, J. Magn. Magn. Mater. **310**, 169 (2007).
[27] R. Sugano, M. Ichimura, S. Takahashi, and S. Maekawa, J. Appl. Phys. **105**, 07D130 (2009).
[28] Ya. B. Bazaliy, B. A. Jones, and S.-C. Zhang, Phys. Rev. B **69**, 094421 (2004).
[29] P. M. Gorley, P. P. Horley, V. K. Dugaev, J. Barnaś, and W. Dobrowolski, J. Appl. Phys. **101**, 034504 (2007).
[30] Y.-T. Cui, G. Finocchio, C. Wang, J. A. Katine, R. A. Buhrman, and D. C. Ralph, Phys. Rev. Lett. **104**, 097201 (2010).